This manuscript is a pre-print and has been submitted for publication in Tectonics. It has not undergone peer-review. If accepted, the final version of this manuscript will be available via the "Peer-reviewed Publication DOI" link on the right hand side of this webpage. Please feel free to contact any of the authors directly.

Inheritance without reactivation: Insights from crustal-scale analogue experiments

Anindita Samsu[1], Alexander R Cruden[1], Nicolas E Molnar[1,2], Roberto F Weinberg[1]

[1]School of Earth, Atmosphere and Environment, Monash University, Clayton, Australia

[2]Tectonics and Geodynamics, RWTH Aachen University, Aachen, Germany

Corresponding author: Anindita Samsu (anindita.samsu@monash.edu)

Key Points

- Analogue models of rifting show for the first time how pervasive basement anisotropies can create complex fault patterns in cover rocks.
- The geometry of basement anisotropies interacts with rift kinematics, impacting fault distributions and orientations.
- Basement anisotropies locally re-orient strain, generating rift-oblique faults in cover rocks.

Abstract

During rifting, pre-existing basement fabrics can affect new faults in cover rocks by a mechanism that does not appear to involve reactivation. This subtle form of inheritance can significantly impact fault network architecture in rift basins above laterally variable basement domains with geomechanical anisotropies. Here we use multi-layer, brittle-ductile, crustal-scale analogue experiments to study the influence of basement anisotropies on fault patterns in the overlying cover during a single phase of orthogonal rifting. The experiments were designed to test whether basement anisotropies, oriented 45° to the extension direction, can lead to the formation of rift faults that are oblique to both the imposed extension direction and basement anisotropies. Our experiments show that a pervasive, vertically layered, mm-wide basement anisotropy creates extension-oblique faults in the overlying cover. We interpret this to arise when local strike-slip kinematics along the interfaces of mechanically contrasting materials in the basement combine with the regional imposed orthogonal extension, creating a transtensional regime. The geometry of basement zones of different mechanical strengths interacts with rift kinematics, impacting the orientation, kinematics and spacing of new faults in the cover. New insights on the influence of pervasive, pre-existing basement fabrics on localized re-orientation of 3D strain in the cover has implications for understanding complex fault systems in rift basins and transfer zones.

1. Introduction

Pre-existing crustal weaknesses commonly influence the location, geometry, orientation, and segmentation of new rifts (Brune et al., 2017; Corti et al., 2007; Daly et al., 1989; Heron et al., 2019; Tommasi & Vauchez, 2001; Wilson, 1966). Many natural rift systems have been impacted by the reactivation of older shear zones, including the NE Brazilian margin (Kirkpatrick et al., 2013), offshore southern Norway (Phillips et al., 2016), the East African Rift System (Daly et al., 1989; Heilman et al., 2019), and the Australian Southern Margin (Gibson et al., 2013; Miller et al., 2002). At the scale of individual rift basins, the architecture of new rift-related faults can be influenced by reactivation of the basement fabric. One widely accepted evidence for reactivation is rift-oblique faults that trend parallel to the strike of the basement fabric (Heilman et al., 2019; Kirkpatrick et al., 2013; Kolawole et al., 2018; Morley et al., 2004; Phillips et al., 2016). However, there are examples of basement-influenced rifting where the role of reactivation can be more ambiguous: In northern Scotland and southeast Australia, Wilson et al. (2010) and Samsu et al. (2019) documented brittle, rift-related structures which are neither parallel with pre-existing basement fabrics nor perpendicular to the inferred direction of regional extension. Variations in the main orientations of these structures were found across areas that overlie basement domains with different metamorphic fabrics. These observations suggest that even when there is no clear evidence of basement reactivation, penetrative basement fabrics can exert some control on the formation of new rift faults.

Faults that are oblique to the extension direction, which we refer to here as "extension-oblique faults", are common features of oblique or transtensional rifts, where strain is accommodated by extension perpendicular to the rift trend and shear parallel to the rift trend (Peace et al., 2018; Withjack & Jamison, 1986). Analogue experiments of oblique rifting have shown that the orientation and kinematics of faults are controlled by the angle of obliquity between the rift trend and the relative displacement direction between the two diverging plates (Agostini et al., 2009; Corti, 2008; Withjack & Jamison, 1986). Corti et al. (2013) and Philippon et al. (2015) proposed that stress re-orientation above a pre-existing weak zone is responsible for extension-oblique faults with dip-slip kinematics at rift margins. These experiments address the influence of an underlying weak zone and the kinematic boundary conditions that lead to extension-oblique faults, but not the role of penetrative basement fabrics in their formation.

The aim of our study is to investigate how penetrative basement anisotropies may influence cover fault orientations during rifting. Here we use crustal-scale analogue models to demonstrate that pre-existing anisotropies in the basement can form extension-oblique faults in the overlying sedimentary cover without normal or oblique reactivation of basement weaknesses. The orientation and kinematics of the faults is controlled by the mechanical properties (e.g., strength) and geometry (i.e., the spacing and width of "weak zones" that create the anisotropy) of the basement.

2. Experimental method

Analogue modelling is a powerful tool for simulating crustal deformation in a controlled environment and testing hypotheses on its tectonic driving mechanisms, using simplified models that are scaled to a practical size (Ranalli, 2001). Our experiments are designed to approximate a foliated basement buried under a sedimentary basin. They were inspired by the western onshore Gippsland Basin, southeast Australia, which formed in the Early Cretaceous during inferred N-S to NNW-SSE regional extension (Ball et al., 2013; Miller et al., 2002; Williams et al., 2011). The western onshore Gippsland Basin overlies two levels of anisotropic basement (Samsu et al., 2020): i) Paleozoic metasedimentary rocks of the Melbourne Zone, with a NNE-SSW trending fabric, which is underlain by ii) an inferred, anomalously strong Neoproterozoic–Cambrian crustal block known as the “Selwyn Block” with a NE-SW structural grain (Cayley et al., 2002; Moore et al., 2016) (Fig. 1). We chose this natural case as a starting point for our experiments because of the availability of multi-scale structural data on the cover and of both of the basement units (Cayley et al., 2002; Moore et al., 2016; Samsu et al., 2019, 2020; Vollgger & Cruden, 2016). We were further motivated to better understand presently unclear relationships between Early Cretaceous rift kinematics, syn-rift fault orientations, and the influence of pre-existing basement weaknesses in the area (Finlayson et al., 1996; Hill et al., 1994, 1995; Samsu et al., 2019).

The simplified experiments represent an area that straddles the postulated eastern boundary of the Selwyn Block, which trends NE-SW beneath the Gippsland Basin (Fig. 1). In the sedimentary cover, faults west of this lateral basement boundary trend NE-SW to ENE-WSW, while faults east of the boundary have a general E-W trend (Fig. 1b). Based on these observations, we designed experiments to simulate how an anisotropic basement, such as the folded and faulted turbidites of the Melbourne Zone or the “strong” Selwyn Block basement, may impact fault patterns in the overlying cover. The models were not designed to explicitly replicate the structural patterns in the Gippsland Basin but rather to provide insight on the influence of basement anisotropies on syn-rift faulting.

2.1. Boundary and initial conditions

All experiments comprised a crustal-scale, brittle-ductile model lithosphere floating isostatically on a fluid model asthenosphere in an acrylic tank (Fig. 2). The tank is 65 cm long, 65 cm wide, and 20 cm deep. The simplified model lithosphere had an initial length and width of 44 cm and 40 cm, respectively, and a thickness of 7 cm (Fig. 3). It consisted of a brittle sedimentary “cover”, a ductile “basement”, and a ductile lithospheric mantle. The model thicknesses scale to natural layer thicknesses estimated from forward modelling of geophysical potential field data (Moore et al., 2016) and seismological models (Gray et al., 1998; Kennett et al., 2013) (Fig. 3 and Table 1). Since we did not intend to force a rift (cf.

Brune et al., 2017; Zwaan and Schreurs, 2017), we did not place a linear “weak zone” seed in the middle of the model.

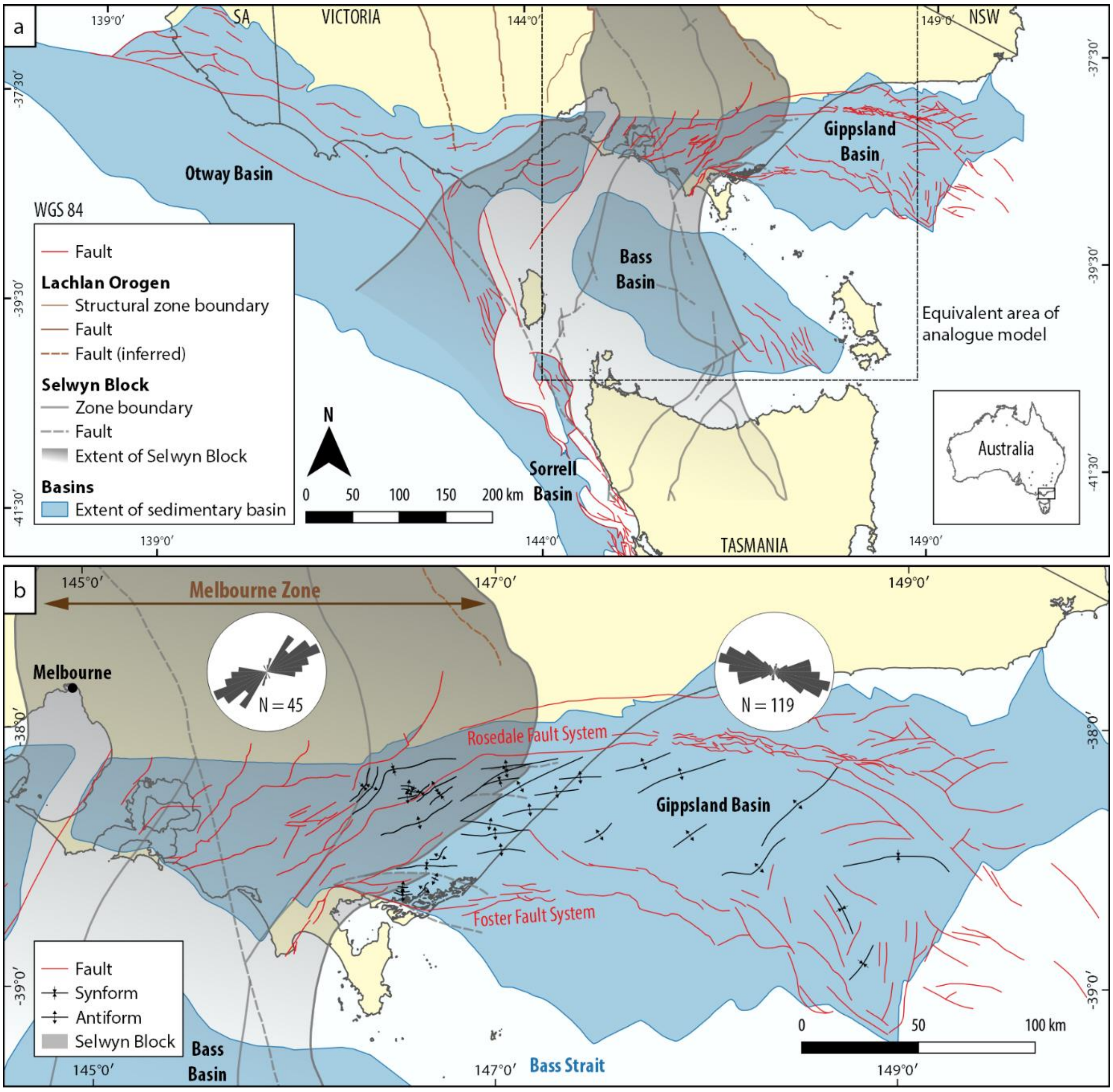

Figure 1 (a) Map of the eastern basins of the Australian Southern Margin rift system, including the Otway, Sorrell, Gippsland, and Bass basins (modified from Samsu et al., 2019). The eastern part of the Otway Basin and the western part of the Gippsland Basin is underlain by the Paleozoic Melbourne Zone (Lachlan Orogen) basement and the Neoproterozoic–Cambrian Selwyn Block basement (Cayley et al., 2002; McLean et al., 2010). (b) Major structures of the Gippsland Basin: The rose diagrams show that faults above the Selwyn Block/Melbourne Zone trend predominantly NE-SW and ENE-WSW, while faults east of this zone trend E-W to NW-SE (modified after Constantine, 2001 and Power et al., 2001).

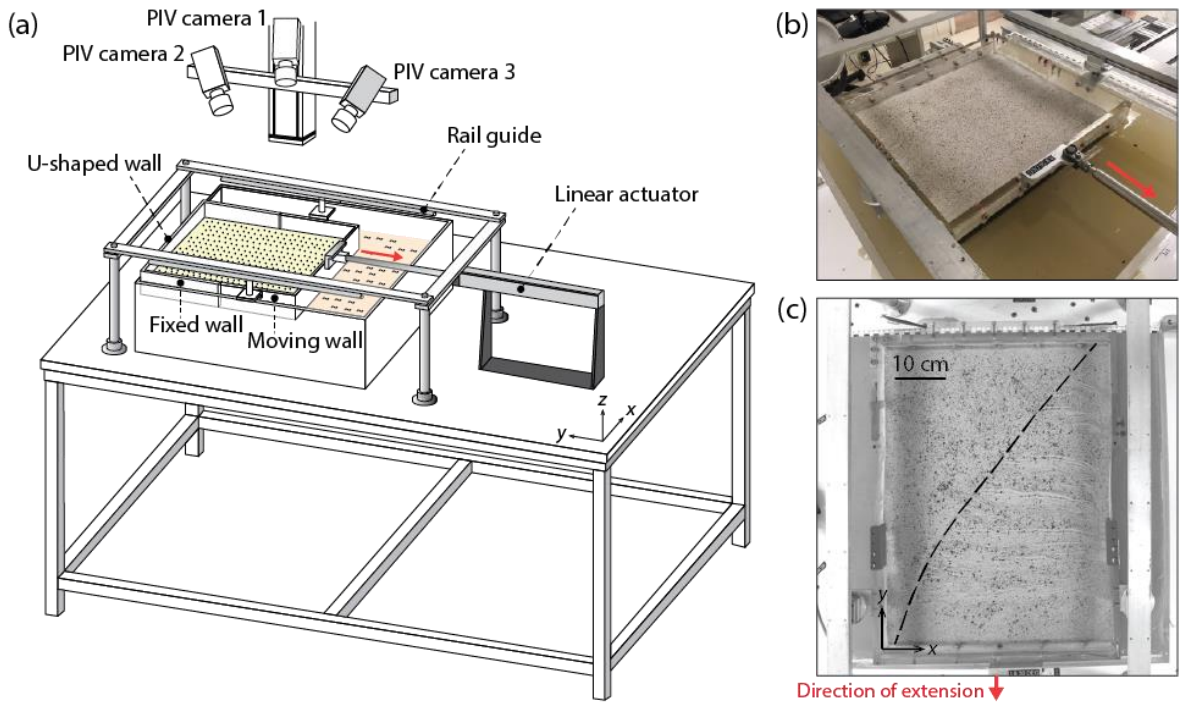

Figure 2 (a) Experimental setup. (b) Oblique view photograph of the model (44 cm long and 40 cm wide) at the start of the experiment. (c) Top view photograph of the model surface (Exp LE-05) at the end of the experiment. The dashed line indicates the final geometry of the strong-normal basement boundary (see Fig. 3 for illustration of basement geometries). In all figures, the red arrow indicates the direction of extension.

One side of the model was attached to a moving wall pulled by a linear actuator, imposing an orthogonal extensional boundary condition that simulates extension similar to that of N-S rifting between Australia and Antarctica in the Early Cretaceous (Ball et al., 2013; Miller et al., 2002). The rate of extension (~4.1 cm/hr) scales to ~2 cm/yr in nature, which is comparable to the divergence rate between Australia and Antarctica at ca. 100 Ma (Müller et al., 2016). The experiments ended after ~42 % extension, by which time the models had been extended ~18.7 cm.

Orthogonal extension boundary conditions ensure that the formation of any faults that are oblique to the extension direction are caused by strength anisotropies in the model crust, as opposed to imposed kinematic boundary conditions. The ductile basement layer was made up of a “strong” and “normal” domain (Fig. 3). The geometries and materials within the strong domain were varied to test their influence on fault patterns in the cover. In Exp LE-01 (the reference experiment) and LE-05, the strong basement was homogeneous. In Exp LE-07 and

LE-08, the strong basement was anisotropic, whereby the width of the anisotropic layers was varied. Boundary effects were expected due to friction between the model's lateral boundaries and the confining U-shaped walls.

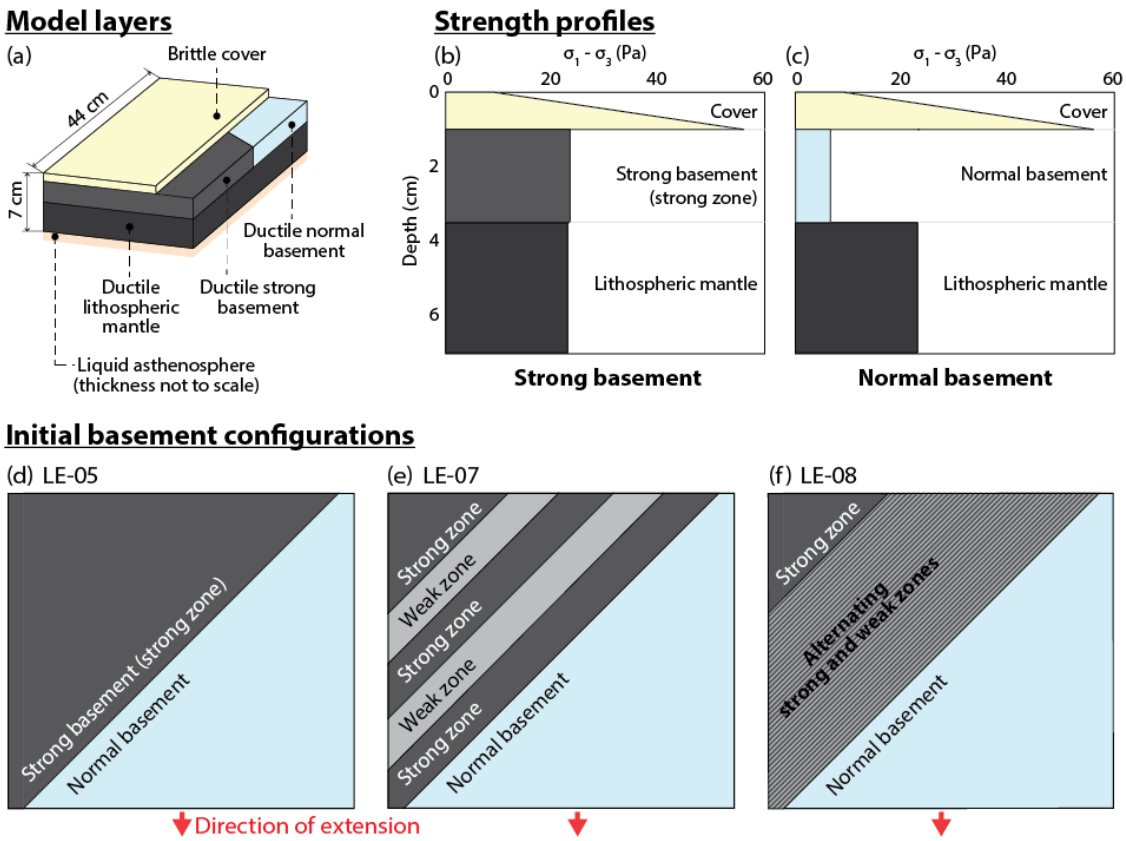

Figure 3 Structure (a) and strength profiles (b-c) of the multi-layer model lithosphere. (d–f) The configuration of the basement at the start of the experiments. The weak zone within the strong basement is only slightly more viscous than the normal basement material.

2.2 Scaling and materials

Model parameters (e.g., length, mass, time, and velocity) and the mechanical properties of the chosen analogue materials were scaled down so that deformation occurred within a convenient time period while still behaving consistently with nature (i.e., the prototype) (Ramberg, 1967). The scaling properties used in the experiments are presented in Table 1.

Table 1 Model scaling parameters and material properties. ESPH = Envirospheres; PDMS = polydimethylsiloxane; WPL = white Plasticine; BPL = black Plasticine; K1 = hollow glass microspheres; NS = Natrosol.

		Thickness		Density		Viscosity		
		Model (mm)	Nature (km)	Model (kg/m^3)	Nature (kg/m^3)	Model (Pa s)	Nature (Pa s)	Material
Normal crust								
Cover	Brittle	10	10	962	2650	-	-	Sand+ESPH
Normal basement	Ductile	25	25	980	2700	4.0×10^4	2.0×10^{21}	PDMS
Strong crust								
Cover	Brittle	10	10	962	2650	-	-	Sand+ESPH
Strong zone (basement)	Ductile	25	25	985	2715	5.7×10^5	2.9×10^{22}	PDMS+WPL+K1
Weak zone (basement)	Ductile	25	25	985	2715	7.3×10^4	3.6×10^{21}	PDMS+WPL+K1
Lithospheric mantle	Ductile	35	35	1067	2940	5.9×10^5	3.0×10^{22}	PDMS+BPL+K1
Asthenosphere	Fluid	-	-	1125	3100	380	1.9×10^{19}	NaCl-NS
Scaling factors: model/nature		$L^* = 1 \times 10^{-6}$		$\rho^* = 3.63 \times 10^{-1}$		$\eta^* = 2.0 \times 10^{-17}$		
Time scaling factor		$t^* = \eta^*/(\rho^* \cdot g^* \cdot L^*)$		$t^* = 5.5 \times 10^{-11}$		1 h in model ~ 2.1 Ma in nature		
Velocity scaling factor		$v^* = l^*/t^*$		$v^* = 1.8 \times 10^4$		41 mm/h in model ~ 20 mm/yr in nature		
Gravity scaling factor		$g^* = g_m/g_p$		$g^* = 1$				
Stress scaling factor		$\sigma^* = \rho^* \cdot L^*$		$\sigma^* = 3.63 \times 10^{-7}$				

A length scaling factor $L^* = L_m/L_p = 1 \times 10^{-6}$ was adopted (subscripts *m* and *p* refer to the model and natural prototype, respectively), so that 1 cm in the model represents 10 km in nature. The 44 cm by 40 cm surface area of the model therefore corresponds to a 440 km × 400 km area in nature (Fig. 1a). The scaling factor for density ρ^* was set to 3.63×10^{-1}. The experiments were run under normal gravitational acceleration, so that the scaling factor for acceleration due to gravity $g^* = 1$, which gives a scaling factor for stress $\sigma^* = \rho^* \times g^* \times L^* = 3.63 \times 10^{-7}$.

A mixture of dry granular materials with a bulk density $\rho_b = \rho_m \approx 960$ kg/m^3 was prepared to approximate a scaled natural density of $\rho_p = 2{,}650$ kg/m^3 for the cover. We used a mixture of dry quartz sand ($\rho_b = 1{,}580$ kg/m^3) and hollow ceramic Envirospheres® BLF and BL150 ($\rho_b \approx 390$ kg/m^3) with mass percentages of ~77.9%, 21.2%, and 1.9%, respectively, similar to Molnar et al. (2017). The internal friction angle $\phi < 38°$ and very low cohesion value $c \sim 9$ Pa of this material, measured by Molnar et al. (2017) using a Hubbert-type shear apparatus, makes it a suitable analogue for modelling the brittle cover with a Mohr-Coulomb behavior (e.g., Byerlee, 1978; Davy & Cobbold, 1991; Mandl et al., 1977; Schellart, 2000). The quartz sand is characterized by a homogeneous grain size distribution, with ~73% of the grains falling in the 150–300 µm range.

We used polydimethylsiloxane (PDMS) and PDMS mixtures to model the ductile basement. PDMS is a transparent, high viscosity, high molecular weight silicone polymer frequently used in analogue modeling (Cruden et al., 2006; Molnar et al., 2017, 2018; Pysklywec & Cruden, 2004). It has a density $\rho_m \approx 980$ kg/m^3, which scales to a natural density $\rho_p \approx$ 2700 kg/m^3. Our PDMS (Wacker Elastomer NA) approximates a Newtonian fluid with a viscosity $\eta \approx 4 \times 10^4$ Pa s. The PDMS mixtures have a slightly non-Newtonian rheology (n > 1) defined by the power law:

$$\sigma^n = v\dot{\varepsilon}$$

where σ is stress, n is the power law exponent of the material, v is a material constant (viscosity prefactor), and $\dot{\varepsilon}$ is the strain rate (Cruden et al., 2006). For example, the power law exponent for the model lithospheric mantle (LM) mixture is $n_{LM} = 1.25$ (Molnar et al., 2017), making it nearly Newtonian.

The basement layer is divided into two domains separated by a vertical interface 45° to the extension direction (Fig. 3d–f), consistent with the orientation of the NE-SW boundary and structural trend of the Selwyn Block in the corresponding area in nature (Fig. 1). One domain of "strong" basement approximates the Selwyn Block. The "strong zone" material within the strong basement (Fig. 3) is a mixture of PDMS, modeling clay (white Colorific Plasticine®), and 3M® K1 hollow glass microspheres (e.g., Cruden et al., 2006; Molnar et al., 2017; Riller et al., 2012). Combining the PDMS with modeling clay increases its effective viscosity and density, while adding glass microspheres reduces its density and increases its effective viscosity. The relative amounts of the three components were adjusted to a mixture with 61.0 vol% PDMS, 16.9 vol% white Plasticine®, and 22.1 vol% microspheres, giving a density $\rho = 985$ kg/m^3 and an effective viscosity of ~ 5.7×10^5 Pa s (at our experimental strain rate of 1.0×10^{-4} s^{-1}) and scaling to a natural density of $\rho = 2715$ kg/m^3 and natural viscosity of 2.9×10^{22} Pa s. The rheological properties of the PDMS mixture were measured using an Anton Paar Physica MCR-301 parallel plate rheometer. The experimental strain rate was estimated by dividing the velocity of the linear actuator (i.e., the rate at which the model was extended) by the total initial model thickness of 7 cm (Benes & Scott, 1996).

The strong zone material is one order of magnitude more viscous than the neighboring "normal" basement domain, which consists of pure PDMS (~ 4.0×10^4 Pa s). Anisotropies within the strong basement are reproduced by incorporating linear "weak zones" (Fig. 3) using a PDMS mixture consisting of 80.9 vol% PDMS, 9.0 vol% white Plasticine®, and

10.1 vol% microspheres. This material has an effective viscosity of ~ 7.3×10^4 Pa s, hence it is only slightly more viscous than the normal basement material.

The model lithospheric mantle is a mixture of 55.8 vol% PDMS, 29.7 vol% modeling clay (black Colorific Plasticine®), and 14.6 vol% 3M® K1 hollow glass microspheres (ρ = 125 kg/m^3). Based on previous analogue modelling of rifting (Molnar et al., 2017), we used a mixture of 55.8 vol% PDMS, 29.7 vol% black Plasticine®, and 14.6 vol% microspheres to achieve a density ρ_m = 1067 kg/m^3 and effective viscosity of 5.9×10^5 Pa s, corresponding to an upscaled density ρ_p = 2940 kg/m^3 and viscosity of 3.0×10^{22} Pa s.

The model asthenosphere is a mixture of Natrosol® 250 HH, NaCl (sodium chloride), formaldehyde, and deionized water (Boutelier et al., 2016; Molnar et al., 2017). Natrosol® hydroxyethylcellulose is a water-soluble polymer that can used to modify the viscosity of an aqueous solution without significantly affecting its density (Boutelier et al., 2016). Natrosol® acts as a Newtonian fluid under shear strain rates typically employed in experimental tectonics (Boutelier et al., 2016). The model asthenosphere mixture has a viscosity μ_m = 380 Pa s, scaling to a prototype viscosity $\mu_p = 1.9 \times 10^{19}$ Pa s, which is comparable with natural viscosity estimates for the asthenosphere (Artyushkov, 1983; Ranalli, 1995). The mixture has a density ρ_m = 1,125 kg/m^3 (Molnar et al., 2017), equivalent to a natural density $\rho_p \approx$ 3,100 kg/m^3 (e.g., Pysklywec and Cruden, 2004).

2.4 Deformation monitoring and analysis

Deformation in the cover layer was monitored during the experiment by stereoscopic particle imaging velocimetry (PIV) (Adam et al., 2005), so that the resulting strain distribution and fault orientations could be characterized over time. The PIV system comprises three high-speed cameras that provide a spatial resolution ≥ 1 mm and a temporal resolution ≥ 0.1 s (Molnar et al., 2017). Successive images were recorded at 15 s intervals during each experimental run. Surface strain and topographic data was derived following the workflow of Molnar et al. (2017). The incremental displacement field was computed using stereo cross correlation, forming the basis for deriving the strain tensor components,

$$E_{ij} = \frac{\partial V_i}{\partial_j} \; with \; i \; \in \{x, y, z\} \; and \; j\{x, y, z\}$$

where E_{ij} describes the gradient in the vector component *i* along the *j* axis (Adam et al., 2005), and *V* is the velocity vector. The scalar fields were used to derive incremental normal and shear strain as well as the height of the model surface, or digital elevation model (DEM). The cumulative strain was calculated as the sum of the incremental strain and used to produce a grid of finite strain ellipses. The maximum normal strain on the surface, E_{surf}, was derived from the larger eigenvalue of the 2D strain matrix

$$\begin{vmatrix} E_{xx} & E_{xy} \\ E_{yx} & E_{yy} \end{vmatrix}$$

and the relationship

$$E_{surf} = \frac{(E_{xx} + E_{yy})}{2} + \sqrt{\frac{\left(E_{xx} + E_{yy}\right)^2}{4} + \frac{\left(E_{xy} + E_{yx}\right)^2}{4}}$$

A local coordinate system was chosen such that the *z*-direction is aligned with the surface normal. *Exx* and *Exy* are partial derivatives of the velocity components $\partial Vx/\partial x$ and $\partial Vx/\partial y$, and *Eyx* and *Eyy* are partial derivatives of the velocity components $\partial Vy/\partial x$ and $\partial Vy/\partial y$. Strain maps, complemented with DEMs and top-view photographs of the model surface (illuminated with oblique lighting) enabled us to track the nucleation, growth, and distribution of faults at different stages of the experiments. The final geometries of the basement anisotropies were documented by photographing the top surface of the basement layer after the granular cover material was removed at the end of each experiment.

3. Results

We present the results of four experiments: Exp LE-01, LE-05, LE-07, and LE-08. When viewing the models in map view, the upper side of the image is referred to as “north”, and the model is being extended towards the “south”. In describing the fault patterns, the cover is divided into two domains: a NW domain, underlain by the strong basement (with or without weak zones), and a SE domain, which overlies the normal basement (Fig. 4). The basement anisotropies were oriented 45° to the extension direction at the start of the experiment and underwent progressive rotation towards ~30°N by the end of the experiment due to stretching of the model. Faults near the western and eastern boundaries of the models curve towards parallelism with the model edges. This boundary effect results from friction between the model’s lateral boundaries and the confining U-shaped walls. It affects a small area outside the central region of interest.

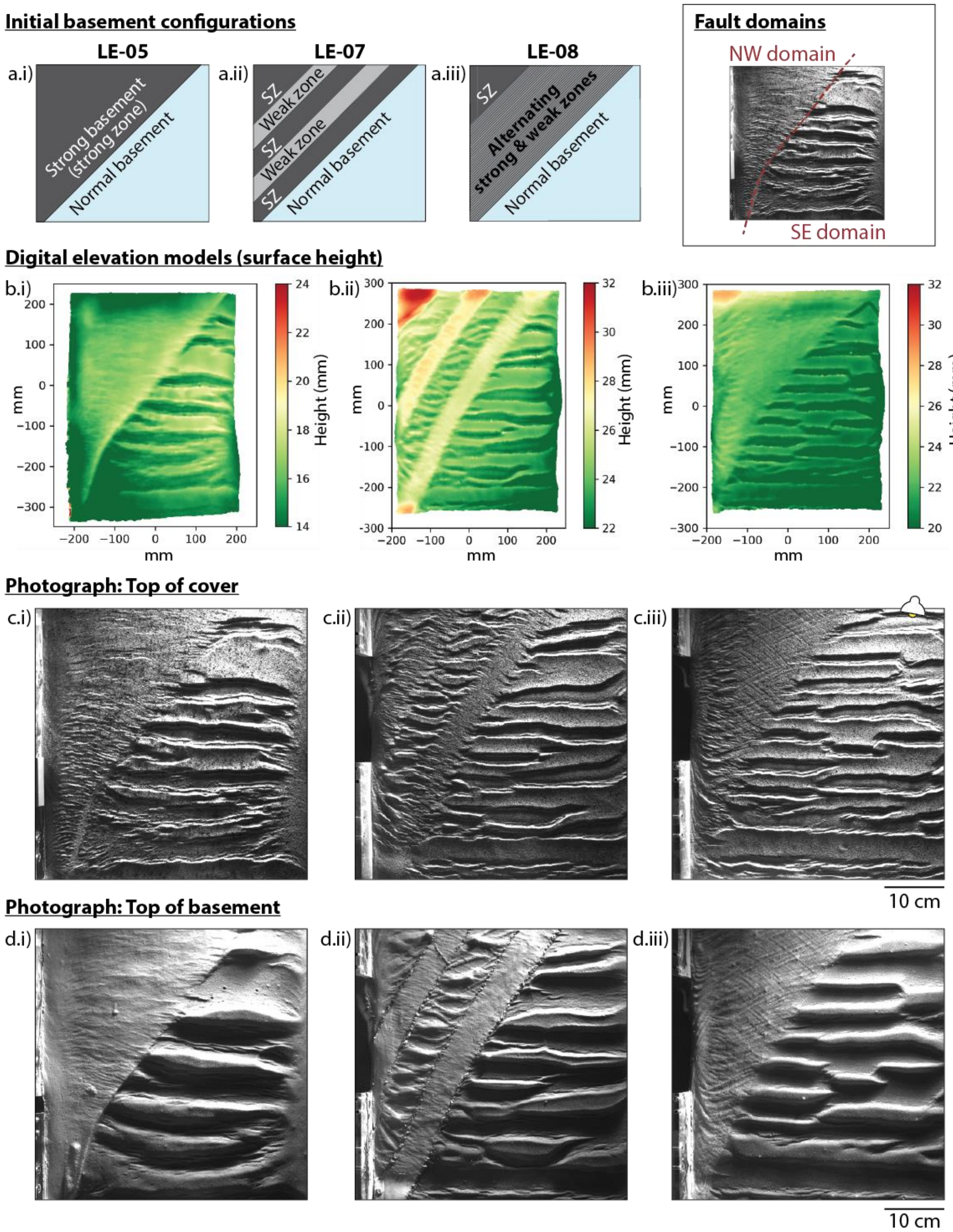

Figure 4 Results of orthogonal extension experiments at 4.5 h (47% strain) in map view, with no anisotropy (a.i), 5.4 cm-wide weak zones (a.ii), and ~2 mm-wide weak zones (a.iii) in the strong basement block. (b) DEM from photogrammetric PIV data. (c) and (d) are top-view photographs of the surface of model (cover) and basement, respectively, with oblique illumination from the top right corner. Larger versions of these photographs are available in the supporting information (Figures S10 to S15). The top right inset shows the position of the NW and SE domains. SZ = strong zone.

3.1 Reference experiment: quasi-homogeneous basement (Exp LE-01)

Our reference experiment (LE-01) shows that even though the two basement domains have different strengths, the style of faulting in the cover is uniform. At the time of running these experiments, we determined that conducting a second control experiment with a uniform basement was not necessary, as it would have led to the same result as Exp LE-01 (see S2 in supporting information).

An E-W trending horst and graben system developed across the entire model area. Based on the DEM, E-W trending normal faults began to nucleate by ~0.3 h (3% extension). As extension progressed, the faults propagated both westwards and eastwards. They reached their final length at ~2 h (21% extension), after which strain was accommodated by widening of the graben. Fault orientation was not influenced by the presence of the oblique strong-normal basement interface. This suggests that the viscosity contrast between the strong basement and normal basement in this experiment was negligible and that a higher viscosity contrast is required for two adjoining rheologically different basement domains to influence the orientation of rift faults during orthogonal extension.

3.2 Strong vs. normal basement (Exp LE-05)

Exp LE-05 involves a homogeneous strong basement, as in Exp LE-01. However, the strong basement material (with an effective viscosity of ~ 5.7×10^5 Pa s) is one order of magnitude more viscous than the adjacent normal basement (~ 4.0×10^4 Pa s). The effect of this strength contrast is apparent in the distinct styles of faulting above the two domains (Fig. 4b.i and 4c.i). The SE domain is characterized by an E-W trending horst and graben system. Strain was localized along oppositely dipping faults which formed at early stages (~0.8 h; 8% strain) and were spaced ~3 to 4 cm apart by the end of the experiment (Movies S4 and S5 in supporting information). The faults reached their final length at ~1.3 h (13% strain), when their lateral propagation was arrested at the model boundary and the diagonal strong-normal basement boundary. As extension progressed, the grabens deepened as throw along the bounding faults increased. Once the boundary faults had propagated to the bottom of the cover, strain was accommodated by widening of the graben.

In the NW domain, strain in the cover was more distributed, resulting in short, <1 mm-spaced faults (Fig. 4c.i). The faults initially formed in the south (~1.4 h; 15% strain) and then began nucleating in the north, near the model center (~2.0 h; 21% strain) as extension progressed. By the end of the experiment, faults above the strong basement had not linked together via relay structures, so that their length remained shorter than the faults in the SE domain (Fig. 4c.i). Most of the faults in the NW domain are E-W, but those within ~30 mm of the strong-normal basement boundary trend WNW-ESE, curving to approach perpendicularity to the boundary.

3.3 Wide anisotropy in the strong basement (Exp LE-07)

The overall evolution and final pattern of faults in the SE domain in Exp LE-07 and LE-08 (Section 3.4) are very similar to the horst-and-graben style of faulting in the SE domain of Exp LE-05. In Exp LE-07, the fault pattern in the NW domain is influenced by the presence of two linear weak zones which are 5.4 cm wide and spaced 5.4 cm apart (Fig. 4a.ii and 5b.ii). Faults above the weak zones form grabens bound by oppositely dipping, E-W trending faults, comparable to the style of faulting in the SE domain (Fig. 4c.ii). The spacing of these faults appears to be intermediate between two end members of fault localization (i.e., highest degree of localization above the normal basement and even distribution above the strong basement). NW-SE trending faults above the strong basement are evenly distributed and narrowly spaced.

In the top view photographs of the model surface (Movie S6 in supporting information), E-W trending faults in the SE domain had begun forming by ~0.8 h (8% strain). E-W trending faults above the weak zones within the NW domain began forming at ~1.1 h (11% strain). Faults above strong zones within the NW domain began forming at ~2.0 h (21% strain), first nucleating at the boundaries of the weak zones and then propagating inwards, orthogonal to the basement domain boundaries.

The formation of NW-SE trending faults above the strong zones and E-W trending faults above the weak zones within the NW domain were controlled by the widely spaced anisotropy in the underlying basement (Fig. 5). This experiment demonstrates that strain partitioning resulted from the presence of extension-oblique zones of highly contrasting strengths, simulated by large viscosity differences in the models. Finite strain ellipses at the end of this experiment exhibit a N-S maximum stretching direction in the SE domain and weak zones in the NW domain (consistent with the imposed N-S extension) and a NNW-SSE maximum stretching direction above the strong basement in the NW domain (Fig. 5a).

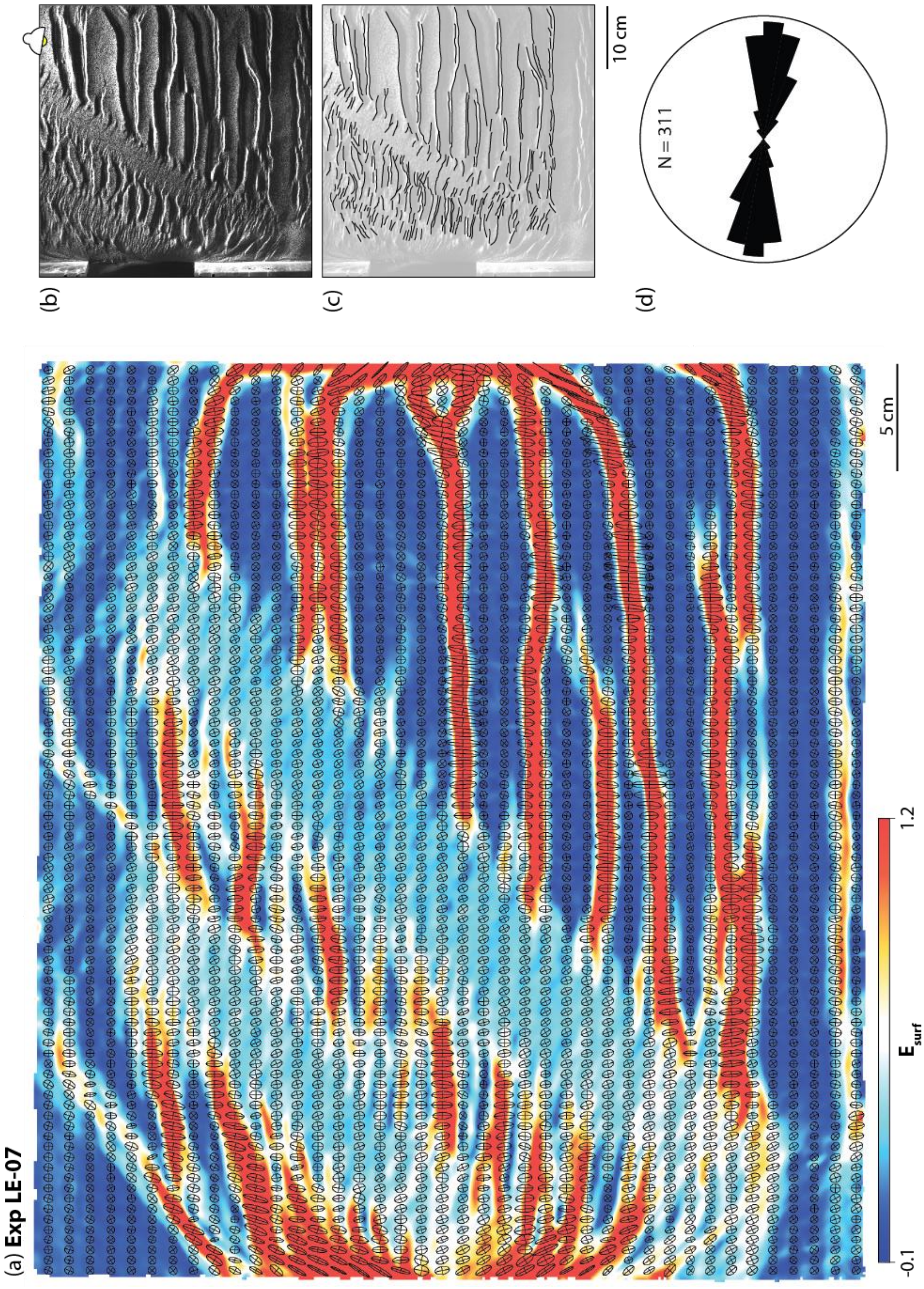

Figure 5 Results from Exp LE-07: (a) cumulative maximum normal strain on surface and 2D strain ellipses at the end of the experiment, plotted at their initial location (t = 0); (b) top view photograph of model surface illuminated at an angle from the north, indicated by the lamp on the figure; (c) fault traces interpreted from photograph of model surface; and (d) rose diagram of fault traces. Note rotation of fault orientation at the boundaries between weak and strong zones. For the evolution of the cumulative strain, see Movie S7 in the supporting information.

3.4 Narrow anisotropy in the strong basement (Exp LE-08)

In Exp LE-08, we implemented a higher degree of anisotropy than in Exp LE-07 by creating narrowly spaced, ~2 mm-wide weak zones within the strong basement, separated by ~2 mm-wide strong basement material (Fig. 4a.iii). In the top view photographs of the model surface (Movie S8 in supporting information), E-W trending faults in the SE domain began forming by ~0.8 h (8% strain). Faults in the NW domain began forming at ~1.4 h (15% strain) near the model's western edge. Two sets of narrowly spaced faults, trending NW-SE and ENE-WSW, began forming at ~3.1 h (32% strain) (Fig. 6b). These coeval fault sets are oblique to the N-S extension direction, the NE-SW trending anisotropy, and the strong-normal basement boundary. The two sets form an apparently conjugate or orthorhombic pattern, with an acute bisector trending WNW-ESE (100°) (Fig. 7b). The obtuse bisector trends NNE-SSW (10°), deviating slightly from the imposed N-S extension. The ENE-WSW trending set is more pronounced than the WNW-ESE trending set because they exhibit greater dip-slip displacement. Finite strain ellipses at the end of this experiment exhibit a N-S maximum stretching direction in the SE domain and a NNW-SSE maximum stretching direction in the NW domain (Fig. 6a).

Although the fault populations in the NW and SE domains exhibit different orientations, both patterns formed as products of the same imposed N-S directed bulk extension (Fig. 6b and 6c). Parallel, E-W trending faults in the SE domain represent extension-orthogonal normal faults that are consistent with formation in an Andersonian normal faulting regime. In contrast, the orthorhombic fault pattern in the NW domain signifies a local change in the 3D strain field due to the role of the pervasive anisotropy in the basement. Because these faults must accommodate the bulk N-S extension, we infer that these oblique fault sets must have a strike-slip component, as indicated in Fig. 6c and 7b.

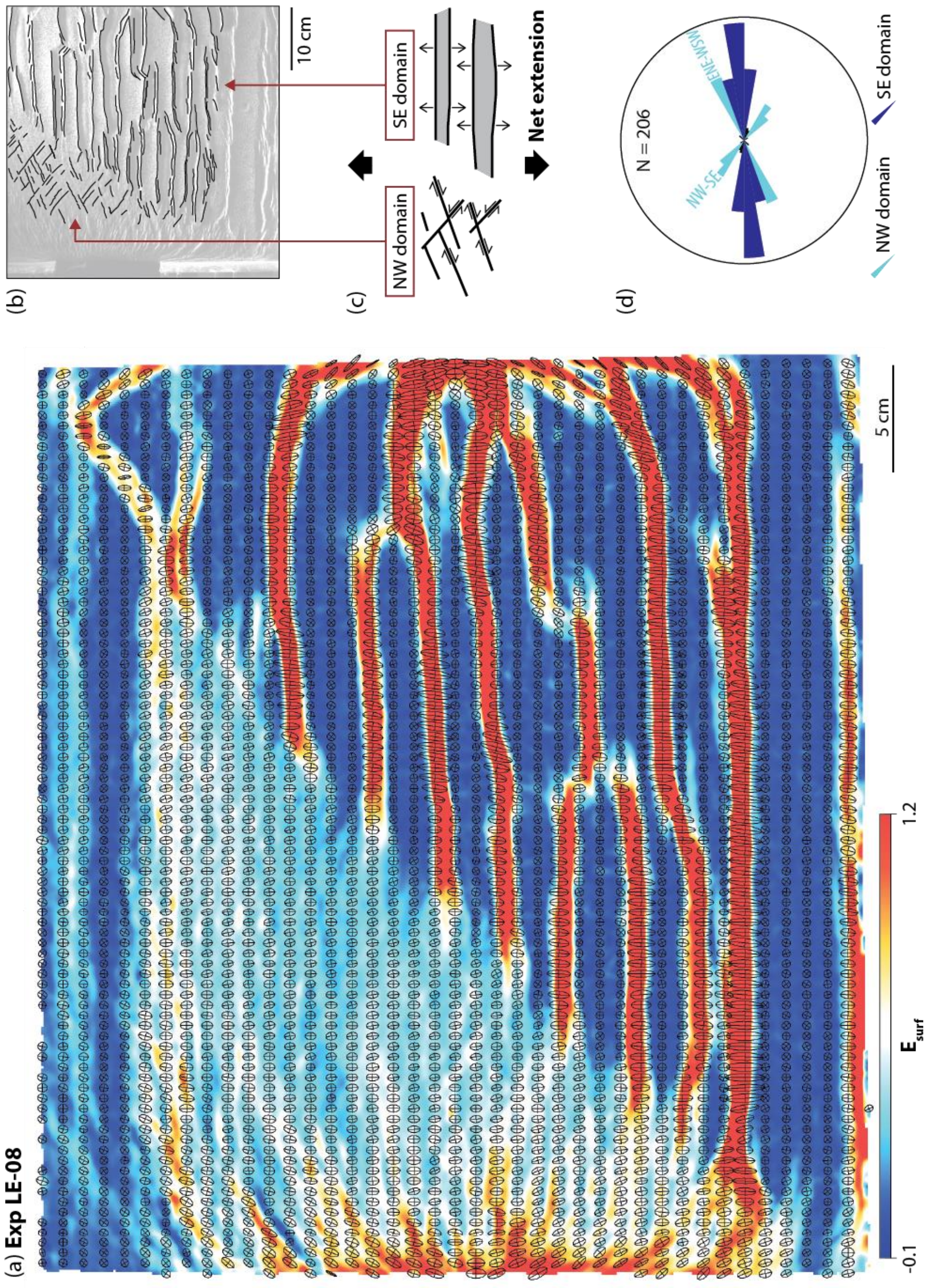

Figure 6 Results from Exp LE-08: (a) cumulative maximum normal strain on surface and 2D strain ellipses at the end of the experiment, plotted at their initial location (t = 0); (b) fault traces overlain on top-down photograph of model surface, (c) schematic plan view illustration of the accommodation of N-S extension by an orthorhombic fault set in the NW domain and E-W faults in the SE domain, and (d) rose diagram of fault traces. For the evolution of the cumulative strain, see Movie S9 in the supporting information.

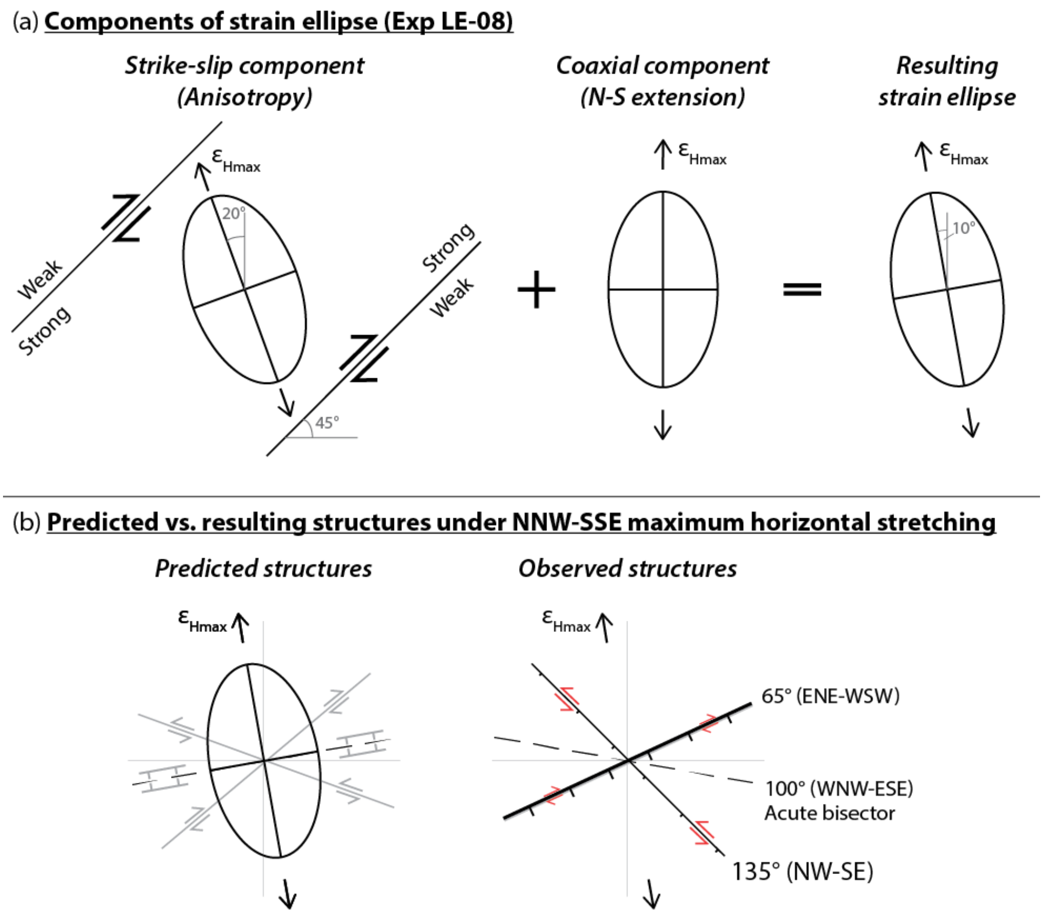

Figure 7 Schematic illustration of deformation and associated kinematics in the NW domain of Exp LE-08. (a) The representative strain ellipse can be broken down into a strike-slip (non-coaxial) and coaxial component. These representative 2D strain ellipses are not to scale; the relative contributions of the strike-slip and coaxial component may be different in the experiment. (b) Comparing the predicted structures (under a NNW-SSE maximum horizontal stretching direction ε_{Hmax}) with the resulting faults at the model surface at the end of the experiment. The reason for this discrepancy is an effect unaccounted for in the simple prediction (see Section 4.3 for explanation). The observed ENE-WSW trending faults are wider than NW-SE faults, suggesting that they have accommodated a significant amount of dip-slip displacement (greater than strike-slip displacement).

4. Discussion

In the experiments, deformation in the cover was influenced by re-orientation of the stress and strain fields across the ductile basement layer, as there were no weak layers that separated the cover and basement materials (cf. "attached stress regime" in Bell, 1996). As a result, faults in the brittle cover were localized above areas of thinning in the ductile basement (compare Fig. 4c and 4d).

4.1 The influence of basement strength on fault spacing

Stronger basement domains in our models correspond with distributed deformation in the overlying cover, while weaker basement domains correspond to localized deformation. In Exp LE-05, the NW domain (above the strong basement) is populated by short, closely spaced faults. The SE domain (above the normal basement) experienced a higher degree of strain localization, evidenced by widely spaced grabens that are bounded by long faults with large displacements (Fig. 4c.i). Similarly in Exp LE-07, the spacing of faults in the NW domain above the weak zones is greater than between faults above the strong zones, but smaller than the spacing between faults in the SE domain (Fig. 4c.ii). These results suggest that fault spacing is controlled by the strength ratio between the ductile and brittle layers (Davy et al., 1995), which is modulated by the viscosity of the ductile basement material.

Our findings are in agreement with previous work on brittle-ductile coupling, which describes the interaction between viscous flow and brittle failure at the horizontal interface between brittle and ductile layers in the continental lithosphere (Ranalli, 1995). The mechanical role of the ductile layer in determining the transition from localized to distributed brittle deformation has been investigated through numerous numerical and analogue experiments of compressional (Riller et al., 2012; Schueller et al., 2005, 2010; Schueller & Davy, 2008) and extensional systems (Bellahsen et al., 2003; Brun, 1999; Sharples et al., 2015; Wijns et al., 2005).

4.2 Rotation of strain axes above a strong, anisotropic basement block

Despite the orthogonal extension boundary condition in our experiments, our models simulate transtension due to the presence of NE-SW trending anisotropies in the basement. The deformation observed in the brittle cover reflects deformation in the underlying basement, which is governed by ductile flow (Fossen & Tikoff, 1998). The obliquity of faults in the NW domain of Exp LE-07 and LE-08 suggests that the model cover did not experience pure shear during extension. Although extension-oblique faults in the NW domain form a small subset of the total fault population, we discuss them at length because their nature reflects the influence of different geometries of basement anisotropies (compare Exp LE-07 and LE-08; Fig. 4).

Calculated finite strain ellipses at the end of Exp LE-08 (Fig. 6a) exhibit a N-S maximum stretching direction ε_{Hmax} in the SE domain. The NW domain is populated by strain ellipses with a NNW-SSE ε_{Hmax}, deviating slightly from N-S. We can explain the rotation of the 2D strain ellipses from N-S to NNW-SSE by the superposition of a coaxial strain component (the N-S imposed extension) and a strike-slip component (Fig. 7a).

For the strike-slip component, we can infer dextral shearing along each strong-weak interface in the basement, as the anisotropies rotated from 45° to ~30°N with increasing extension (Fig. 4). As shown in Fig. 7a and 8, dextral motion along strong-weak interfaces results in internal sinistral shearing within each narrow strong zone, consistent with the anti-clockwise rotation of the strain ellipses. This same strain ellipse rotation is also demonstrated in Exp LE-07 within each strong zone in the NW domain (Fig. 5a).

From the NNW-SSE trending ε_{Hmax}, we expected ENE-WSW trending normal faults or a conjugate set of faults with an ENE-WSW trending acute bisector to form in the NW domain (Fig. 7b). Instead, strain in this domain is accommodated by an orthorhombic fault system, where the ENE-WSW set is dominant. We infer that the ENE-WSW faults have a significant dip-slip and minor strike-slip offsets. A less dominant NW-SE fault set with a significant strike-slip component and a minor dip-slip component must also form to maintain strain compatibility (e.g., Fossen & Tikoff, 1998). The reason for the discrepancy between the observed and predicted fault patterns is outlined in detail in Section 4.3.

The presence of alternating 5.4 cm-wide strong and weak zones in the NW domain of Exp LE-07 resulted in strain partitioning. ε_{Hmax} trends N-S above the weak zones within the NW domain (Fig. 5), resulting in E-W trending faults. The NNW-SSE trending ε_{Hmax} is confined to the strong zones. In this experiment, E-W trending faults first nucleated and propagated in the SE domain and in the weak zones of the NW domain until they reached the interfaces with the strong zones; NW-SE trending faults then propagated from the interfaces and into the center of the strong zones. We interpret that the strong zones acted as transfer zones (cf. Zwaan and Schreurs, 2017), across which older faults in the SE domain and in the NW domain weak zones linked up via extension-oblique faults (Fig. 8a). To maintain strain compatibility, these NW-SE trending faults are likely to have a sinistral strike-slip component. The change in structural style of faults as they propagate laterally from the weak to strong zones is comparable with observations from seismic reflection data from the Great South Basin, New Zealand (Phillips & McCaffrey, 2019). Here, a strong granitic laccolith appears to inhibit the propagation of extension-orthogonal normal faults from the sedimentary unit, causing the fault system to splay before reaching the boundary between the mechanically contrasting units.

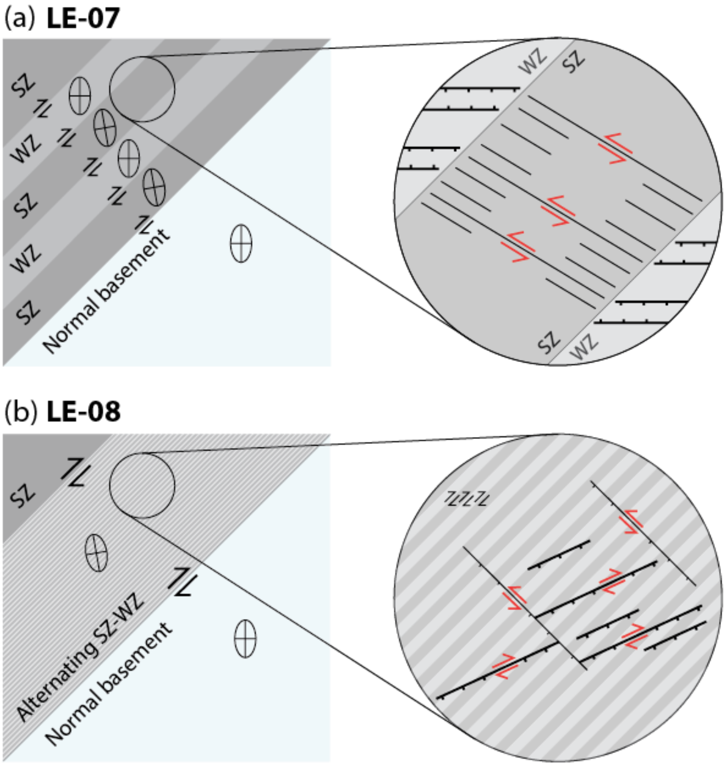

Figure 8 (a) Strain partitioning in the NW domain of Exp LE-07. The 2D strain ellipses reflect N-S maximum horizontal stretching in the normal basement and in the weak zones within the strong basement. In the strong zones, they are rotated anticlockwise. (b) Strike-slip movement along all strong-weak interfaces in the NW domain of Exp LE-08 results in an "averaging effect" of the anisotropic properties of the basement. Hence the strain ellipse is rotated anticlockwise across the entire NW domain. SZ= strong zone; WZ = weak zone.

Strain re-orientation has been observed in lithospheric-scale analogue models where a single pre-existing weakness in the ductile lower crust has an obliquity up to 45° relative to the imposed extension (Philippon et al., 2015). In these models, faults in the brittle upper crust above the strong-weak interface (i.e., so-called "border faults") exhibit dip-slip kinematics even though their trends are oblique to the extension direction. Re-orientation of the extension direction is not apparent for obliquities greater than 45°, and thus strain re-orientation plays a smaller role in fault pattern development, as faults display predominantly oblique-slip kinematics (Agostini et al., 2009). According to Philippon and Corti (2016), the proposed 45° obliquity threshold which determines either strain re-orientation or partitioning must be investigated further. They also noted that the strain re-orientation/partitioning threshold could be controlled by the initial width of the pre-existing weakness. Our experiments, in which all of the basement anisotropies had an initial 45° orientation, confirm that strain re-orientation and partitioning are modulated by the width and spacing of the anisotropies, which we discuss in the next section. However, our models also generated fault patterns and kinematics that differ from previous models (e.g., Agostini et al., 2009; Corti et al., 2013; Philippon et al., 2015; Philippon & Corti, 2016) as we embedded multiple weak zones in the ductile layer to simulate a pervasive fabric.

4.3 The scale-dependent role of basement anisotropies on fault patterns

The different characteristics of extension-oblique faults in Exp LE-07 (above the strong zones in the NW domain) and LE-08 are attributed to the geometry of the basement anisotropies, which interacted with the imposed boundary conditions. While certain structures would have been expected given the NNW-SSE maximum horizontal stretching (Fig. 7b), the role, kinematics and intensity of faults above the different strong and weak regions were modified by: (i) the 45° angle between the imposed N-S stretching and the boundaries between strong and weak zones, along which local strike-slip movement occurred (Fig. 8), and (ii) the spacing and width of the alternating strong and weak zones. This geometric influence is exemplified by faults in the NW domain of Exp LE-07 (Fig. 5). Here, E-W trending faults above the weak zones forced the dominance of NW-SE trending transfer faults above the strong zones, which link the E-W faults and accommodate extensional strain.

Exp LE-07 and LE-08 represent two end-member scenarios where either: a) strain is partitioned between zones of contrasting strength within an anisotropic basement block (Fig. 8a), or b) the properties of zones of contrasting strength are “averaged” (Fig. 8b). Exp LE-08 demonstrates that a basement block, with a stronger average viscosity than the adjacent block and containing a vertical, closely spaced, and pervasive anisotropy, will behave as a single block (Fig. 8b). When the width of the alternating weak and strong zones is below a certain threshold, rotation of the strain axes occurs not just at the strong-weak zone interfaces, but across the entire NW domain. When the width of the anisotropy is increased, alternating weak and strong zones within the strong basement act as discrete basement blocks with their own distinct mechanical properties. Quantifying the threshold width of the anisotropies is beyond the scope of this study, but it is likely to be controlled by the viscosity ratio between the strong and weak zones, the ratio between the brittle crust thickness and the width of the anisotropy, and the minimum resolvable fault displacement in the experimental setup.

4.4 Model limitations and implications for natural rift basins

Our simplified experiments show that localized strain re-orientation above an anisotropic basement, oblique to the extension direction, is responsible for complex fault patterns in the cover. They also demonstrate that a sufficiently anisotropic basement creates transtension, leading to non-Andersonian, extension-oblique faulting. Here we draw comparisons to the natural case of the Gippsland Basin, which inspired our model design, and discuss the potential contributions of our work to understanding structural inheritance in other rift basins.

The starting point for our experimental setup was the enigmatic pattern of Early Cretaceous syn-rift faulting across the Gippsland Basin, attributed to an anomalously strong, heterogeneous, anisotropic lower crustal block (i.e., the Selwyn Block; Cayley et al., 2002; Moore et al., 2016)). The influence of the Selwyn Block is evident in the eastern Otway Basin and western Gippsland Basin, where NE-SW to ENE-WSW trending Early Cretaceous faults are present in the overlying cover (Constantine, 2001; Moore et al., 2000; Norvick & Smith, 2001; Samsu et al., 2019; Willcox et al., 1992) (Fig. 1). This fault set is oblique to the inferred N-S or NNE-SSW direction of regional extension (e.g., Etheridge et al., 1985; Miller et al., 2002; Willcox and Stagg, 1990) . It is also oblique to E-W trending orthogonal rift faults that typify areas beyond the boundaries of the Selwyn Block (Fig. 1b). Power et al. (2001, 2003) attributed this obliquity to transtension arising from NNW-SSE directed oblique extension in the Early Cretaceous, based on seismic reflection data from the eastern (offshore) Gippsland Basin (Fig. 1b). Samsu et al. (2019, 2020) used field observations and potential field geophysical data from the western onshore Gippsland Basin to determine that NE-SW to ENE-WSW syn-rift faults are at acute angles to a strong, subvertical NNE-SSW trending fabric in Paleozoic basement rocks of the Melbourne Zone and the NE-SW structural grain of the Selwyn Block (Moore et al., 2016). Our experiments suggest that while transtension could account for the obliquity of some of the faults in the Gippsland Basin, it may reflect the influence of Melbourne Zone or Selwyn Block basement fabrics on fault kinematics. From Exp LE-05 and LE-08, we also deduced that it is the pervasive fabric within an anomalously strong basement block, and not the lateral boundary between strong and normal basement, which likely produced extension-oblique rift faults across a wide area (Fig. 1 and 4).

The experimental results do not fully replicate fault patterns in the Gippsland Basin. For instance, basin-scale (>1 km long) ENE-WSW trending normal faults in the western onshore Gippsland Basin (Samsu et al., 2019) are comparable to ENE-WSW trending faults in the NW domain of Exp LE-08. However, this part of the model also contains NW-SE trending faults which are not represented in the basin-scale fault map (Fig. 1). Given the imposed N-S bulk extension in the experiment, strain compatibility required the development of the NW-SE trending conjugate fault set once the ENE-WSW trending faults formed. If such NW-SE faults were present in the Gippsland Basin, their strike-slip and dip-slip displacement may have been too small to generate gravity and magnetic anomalies.

The Gippsland Basin could have been exposed to other boundary conditions, such as oblique rifting and an extension direction that is not exactly N-S. Different degrees of rheological contrasts and reactivation of pre-existing faults in the Melbourne Zone and Selwyn Block basement units may have also influenced faulting. Finally, the brittle cover in the natural case is heterogeneous, unlike the homogeneous cover in our models. All of these added complexities in nature would have resulted in fault patterns that are different from those in our experiments.

Despite the simplicity of our experiments, they provide insight as to how an underlying basement anisotropy could generate rift-oblique faults without the direct reactivation of pre-existing weaknesses. They also demonstrate the influence of a strong, anisotropic oblique crustal block on rift basin architecture. The results differ from the more widely explored role of crustal weaknesses (e.g., Autin et al., 2013; Bellahsen and Daniel, 2005; Corti, 2004; Faccenna et al., 1995; Henza et al., 2011, 2010). They show that oblique kinematics (Withjack & Jamison, 1986) are not necessarily required to form extension-oblique faults. All that is needed is a basement that is sufficiently anisotropic, and this anisotropy does not have to occur at the whole of lithosphere scale (cf. Agostini et al., 2009; Brune et al., 2017; Corti, 2008). Our findings support the statement that the local strain direction indicated by individual faults need not reflect the orthogonal extension boundary condition, as previously shown by Philippon et al. (2015).

The influence of basement anisotropies on local strain re-orientation has implications for understanding complex fault systems within transfer zones, where far-field extension vectors and pre-existing basement anisotropies are likely to be oblique (Wilson et al., 2010). Reactivation of basement structures often play a role in the development of transfer zones (Daly et al., 1989; Morfley et al., 2004), and this was thought to be the case in the North Coast Transfer Zone (NCTZ), Scotland. However, Wilson et al. (2010) noted that evidence for reactivation is not as prevalent in the onshore areas of the NCTZ as had been previously implied (Holdsworth, 1989; Roberts & Holdsworth, 1999). Wilson et al. (2010) also showed that fault patterns change across regions with different orientations of pre-existing basement fabrics and that these are oblique to the far-field extension direction. Variations in fault orientations were attributed to a subtle basement influence that generated localized changes in 3D transtensional strains. Our experiments support this hypothesis by showing that local extension directions are re-oriented from the far-field extension direction when the basin is underlain by different anisotropic basement domains. This is the case even when the basement fabrics themselves are not reactivated. While previous analogue experiments have provided insight into the influence of a single basement weakness on the formation, geometry, and orientation of transfer zones (e.g., Acocella et al., 1999; Zwaan & Schreurs, 2017), pervasive anisotropies should be incorporated into the basement to model complex, basin-scale fault systems within transfer zones.

Future experiments may require the use of finer-grained granular material to represent the cover and higher resolution particle tracking to enable direct observation of fault kinematics (cf. Philippon et al., 2015). Such a setup would allow us to make direct comparisons with observed fault kinematics in the natural setting. Our models also used a ductile layer to model "basement" anisotropies. In contrast, basement rocks in nature could have anisotropies that formed during ductile deformation but have entered the brittle regime by the time rifting occurred. There are practical challenges with introducing anisotropies in brittle material, but it is worth considering to understand how a brittle anisotropic basement would influence rift faulting in the cover.

5. Conclusions

The experimental results presented here describe the control of crustal strength on fault spacing and the length scale-dependent relationship between basement anisotropies and fault behavior in the cover during a single phase of rifting. How lateral strength anisotropies in the basement influence fault orientations in the cover is a function of: (i) scale (i.e., the width and spacing of anisotropies relative to the size of the modelled area), and (ii) the mechanical properties of the individual zones that make up the anisotropic material. Hence the geometry of basement domains of differing strengths and variable fabric orientation may interact with rift kinematics, impacting the orientation, kinematics, and spacing of faults in a basin. We show that the basement of a rift basin must be sufficiently anisotropic for extension-oblique rift faults to form across a wide area. Additionally, such faults can form oblique to the trend of pre-existing basement anisotropies, demonstrating that pre-existing basement structures/weaknesses can be inherited via a mechanism other than reactivation, which would otherwise result in new faults that are parallel to these basement structures.

Acknowledgments

The authors thank Steven Micklethwaite for helpful discussions during the preparation of this manuscript. Alexander Peace and an anonymous reviewer are also thanked for constructive reviews of an earlier version of the manuscript. A. Samsu was supported by a Monash University Faculty of Science Dean's International Postgraduate Research Scholarship and Postgraduate Publication Award. Data archiving is underway. Photographs, digital elevation models, strain maps, and structural data used for this contribution are reported in the manuscript and supporting information for review purposes and will be made publicly available on bridges.monash.edu.

References

Acocella, V., Faccenna, C., Funiciello, R., & Rossetti, F. (1999). Sand-box modelling of basement-controlled transfer zones in extensional domains. *Terra Nova*, *11*(4), 149–156. https://doi.org/10.1046/j.1365-3121.1999.00238.x

Adam, J., Urai, J. L., Wieneke, B., Oncken, O., Pfeiffer, K., Kukowski, N., et al. (2005). Shear localisation and strain distribution during tectonic faulting—new insights from granular-flow experiments and high-resolution optical image correlation techniques. *Journal of Structural Geology*, *27*(2), 283–301. https://doi.org/10.1016/j.jsg.2004.08.008

Agostini, A., Corti, G., Zeoli, A., & Mulugeta, G. (2009). Evolution, pattern, and partitioning of deformation during oblique continental rifting: Inferences from lithospheric-scale centrifuge models. *Geochemistry, Geophysics, Geosystems*, *10*(11). https://doi.org/10.1029/2009GC002676

Artyushkov, E. V. (1983). *Geodynamics*. Amsterdam: Elsevier.

Autin, J., Bellahsen, N., Leroy, S., Husson, L., Beslier, M. O., & D'Acremont, E. (2013). The role of structural inheritance in oblique rifting: Insights from analogue models and application to the Gulf of Aden. *Tectonophysics*, *607*, 51–64. https://doi.org/10.1016/j.tecto.2013.05.041

Ball, P., Eagles, G., Ebinger, C., McClay, K., & Totterdell, J. (2013). The spatial and temporal evolution of strain during the separation of Australia and Antarctica. *Geochemistry, Geophysics, Geosystems*, *14*(8), 2771–2799. https://doi.org/10.1002/ggge.20160

Bell, J. S. (1996). Petro geoscience 2. In situ stresses in sedimentary rocks (part 2): Applications of stress measurements. *Geoscience Canada*.

Bellahsen, N., & Daniel, J. M. (2005). Fault reactivation control on normal fault growth: An experimental study. *Journal of Structural Geology*, *27*(4), 769–780. https://doi.org/10.1016/j.jsg.2004.12.003

Bellahsen, N., Daniel, J. M., Bollinger, L., & Burov, E. (2003). Influence of viscous layers on the growth of normal faults: Insights from experimental and numerical models. *Journal of Structural Geology*, *25*(9), 1471–1485. https://doi.org/10.1016/S0191-8141(02)00185-2

Benes, V., & Scott, S. D. (1996). Oblique rifting in the Havre Trough and its propagation into the continental margin of New Zealand: Comparison with analogue experiments. *Marine Geophysical Research*, *18*(2–4), 189–201. https://doi.org/10.1007/BF00286077

Boutelier, D., Cruden, A., & Saumur, B. (2016). Density and visco-elasticity of Natrosol 250 HH solutions: Determining their suitability for experimental tectonics. *Journal of Structural Geology*, *86*, 153–165. https://doi.org/10.1016/j.jsg.2016.03.001

Brun, J. P. (1999). Narrow rifts versus wide rifts: Inferences for the mechanics of rifting from laboratory experiments. *Philosophical Transactions of the Royal Society A: Mathematical, Physical and Engineering Sciences*, *357*(1753), 695–712.

https://doi.org/10.1098/rsta.1999.0349

Brune, S., Corti, G., & Ranalli, G. (2017). Controls of inherited lithospheric heterogeneity on rift linkage: Numerical and analogue models of interaction between the Kenyan and Ethiopian rifts across the Turkana depression. *Tectonics*, 1–20. https://doi.org/10.1002/2017TC004739

Byerlee, J. (1978). Friction of rocks. *Pure and Applied Geophysics*, *116*(4–5), 615–626. https://doi.org/10.1007/BF00876528

Cayley, R. A., Taylor, D. H., VandenBerg, A. H. M., & Moore, D. H. (2002). Proterozoic - Early Palaeozoic rocks and the Tyennan Orogeny in central Victoria: The Selwyn Block and its tectonic implications. *Australian Journal of Earth Sciences*, *49*(2), 225–254. https://doi.org/10.1046/j.1440-0952.2002.00921.x

Constantine, A. (2001). *Sedimentology, Stratigraphy and Palaeoenvironment of the Upper Jurassic-Lower Cretaceous Non-Marine Strzelecki Group, Gippsland Basin, Southeastern Australia*. Monash University. PhD Thesis.

Corti, G. (2004). Centrifuge modelling of the influence of crustal fabrics on the development of transfer zones: Insights into the mechanics of continental rifting architecture. *Tectonophysics*, *384*, 191–208. https://doi.org/10.1016/j.tecto.2004.03.014

Corti, G. (2008). Control of rift obliquity on the evolution and segmentation of the main Ethiopian rift. *Nature Geoscience*, *1*(4), 258–262. https://doi.org/10.1038/ngeo160

Corti, G., van Wijk, J., Cloetingh, S., & Morley, C. K. (2007). Tectonic inheritance and continental rift architecture: Numerical and analogue models of the East African Rift system. *Tectonics*, *26*(6), 1–13. https://doi.org/10.1029/2006TC002086

Corti, G., Philippon, M., Sani, F., Keir, D., & Kidane, T. (2013). Re-orientation of the extension direction and pure extensional faulting at oblique rift margins: Comparison between the Main Ethiopian Rift and laboratory experiments. *Terra Nova*, *25*(5), 396–404. https://doi.org/10.1111/ter.12049

Cruden, A. R., Nasseri, M. H. B., & Pysklywec, R. (2006). Surface topography and internal strain variation in wide hot orogens from three-dimensional analogue and two-dimensional numerical vice models. *Geological Society Special Publications*, *253*(1), 79–104. https://doi.org/10.1144/GSL.SP.2006.253.01.04

Daly, M. C., Chorowicz, J., & Fairhead, J. D. (1989). Rift basin evolution in Africa: the influence of reactivated steep basement shear zones. *Geological Society, London, Special Publications*, *44*(1), 309–334. https://doi.org/10.1144/GSL.SP.1989.044.01.17

Davy, P, Hansen, A., Bonnet, E., & Zhang, S.-Z. (1995). Localization and fault growth in layered brittle-ductile systems: Implications for deformations of the continental lithosphere. *Journal of Geophysical Research: Solid Earth*, *100*(B4), 6281–6294. https://doi.org/10.1029/94JB02983

Davy, Ph, & Cobbold, P. R. (1991). Experiments on shortening of a 4-layer model of the continental lithosphere. *Tectonophysics*, *188*(1–2), 1–25. https://doi.org/10.1016/0040-1951(91)90311-F

Etheridge, M. A., Branson, J. C., & Stuart-Smith, P. G. (1985). Extensional basin-forming structures in Bass Strait and their importance for hydrocarbon exploration. *The APEA Journal*, *25*, 344–361.

Faccenna, C., Nalpas, T., Brun, J. P., Davy, P., & Bosi, V. (1995). The influence of pre-existing thrust faults on normal fault geometry in nature and in experiments. *Journal of Structural Geology*, *17*(8), 1139–1149. https://doi.org/10.1016/0191-8141(95)00008-2

Finlayson, D. M., Johnstone, D. W., Owen, A. J., & Wake-Dyster, K. D. (1996). Deep seismic images and the tectonic framework of early rifting in the Otway Basin, Australian southern margin. *Tectonophysics*, *264*(1–4), 137–152. https://doi.org/10.1016/S0040-1951(96)00123-0

Fossen, H., & Tikoff, B. (1998). Extended models of transpression and transtension, and application to tectonic settings. *Geological Society, London, Special Publications*, *135*(1), 15–33. https://doi.org/10.1144/GSL.SP.1998.135.01.02

Gibson, G. M., Totterdell, J. M., White, L. T., Mitchell, C. H., Stacey, A. R., Morse, M. P., & Whitaker, A. (2013). Pre-existing basement structure and its influence on continental rifting and fracture zone development along Australia's southern rifted margin. *Journal of the Geological Society*, *170*(2), 365–377. https://doi.org/10.1144/jgs2012-040

Gray, D. R., Foster, D. A., Gray, C., Cull, J., & Gibson, G. (1998). Lithospheric Structure of the Southeast Australian Lachlan Orogen along the Victorian Global Geoscience Transect. *International Geology Review*, *40*(12), 1088–1117.

https://doi.org/10.1080/00206819809465256

Heilman, E., Kolawole, F., Atekwana, E. A., & Mayle, M. (2019). Controls of Basement Fabric on the Linkage of Rift Segments. *Tectonics*, *38*(4), 1337–1366. https://doi.org/10.1029/2018TC005362

Henza, A. A., Withjack, M. O., & Schlische, R. W. (2010). Normal-fault development during two phases of non-coaxial extension: An experimental study. *Journal of Structural Geology*, *32*(11), 1656–1667. https://doi.org/10.1016/j.jsg.2009.07.007

Henza, A. A., Withjack, M. O., & Schlische, R. W. (2011). How do the properties of a pre-existing normal-fault population influence fault development during a subsequent phase of extension? *Journal of Structural Geology*, *33*(9), 1312–1324. https://doi.org/10.1016/j.jsg.2011.06.010

Heron, P. J., Peace, A. L., McCaffrey, K. J. W., Welford, J. K., Wilson, R., Hunen, J., & Pysklywec, R. N. (2019). Segmentation of Rifts Through Structural Inheritance: Creation of the Davis Strait. *Tectonics*, *38*(7), 2411–2430. https://doi.org/10.1029/2019TC005578

Hill, K. A., Cooper, G. T., Richardson, M. J., & Lavin, C. J. (1994). Structural framework of the Eastern Otway basin: inversion and interaction between two major structural provinces. *Exploration Geophysics*. https://doi.org/10.1071/EG994079

Hill, K. A., Finlayson, D. M., Hill, K. C., & Cooper, G. T. (1995). Mesozoic tectonics of the Otway Basin region: the legacy of Gondwana and the active Pacific margine — a review and ongoing research. *The APPEA Journal*, *35*(1), 467–493. https://doi.org/https://doi.org/10.1071/AJ94030

Holdsworth, R. E. (1989). Late brittle deformation in a caledonian ductile thrust wedge: new evidence for gravitational collapse in the Moine Thrust sheet, Sutherland, Scotland. *Tectonophysics*, *170*(1–2), 17–28. https://doi.org/10.1016/0040-1951(89)90100-5

Kennett, B. L. N., Fichtner, A., Fishwick, S., & Yoshizawa, K. (2013). Australian seismological referencemodel (AuSREM): Mantle component. *Geophysical Journal International*, *192*(2), 871–887. https://doi.org/10.1093/gji/ggs065

Kirkpatrick, J. D., Bezerra, F. H. R., Shipton, Z. K., Do Nascimento, A. F., Pytharouli, S. I., Lunn, R. J., & Soden, A. M. (2013). Scale-dependent influence of pre-existing basement shear zones on rift faulting: a case study from NE Brazil. *Journal of the Geological Society*, *170*, 237–247. https://doi.org/10.1144/jgs2012-043

Kolawole, F., Atekwana, E. A., Laó-Dávila, D. A., Abdelsalam, M. G., Chindandali, P. R., Salima, J., & Kalindekafe, L. (2018). Active Deformation of Malawi Rift's North Basin Hinge Zone Modulated by Reactivation of Preexisting Precambrian Shear Zone Fabric. *Tectonics*, *37*(3), 683–704. https://doi.org/10.1002/2017TC004628

Mandl, G., Jong, L. N. J., & Maltha, A. (1977). Shear zones in granular material. *Rock Mechanics*, *9*(2–3), 95–144. https://doi.org/10.1007/BF01237876

McLean, M. A., Morand, V. J., & Cayley, R. A. (2010). Gravity and magnetic modelling of crustal structure in central Victoria: what lies under the Melbourne Zone? *Australian Journal of Earth Sciences*, *57*(2), 153–173. https://doi.org/10.1080/08120090903416245

Miller, J. M. L., Norvick, M. S., & Wilson, C. J. L. (2002). Basement controls on rifting and the associated formation of ocean transform faults - Cretaceous continental extension of the southern margin of Australia. *Tectonophysics*, *359*(1–2), 131–155. https://doi.org/10.1016/S0040-1951(02)00508-5

Molnar, N. E., Cruden, A. R., & Betts, P. G. (2017). Interactions between propagating rotational rifts and linear rheological heterogeneities: Insights from three-dimensional laboratory experiments. *Tectonics*, *36*(3), 420–443. https://doi.org/10.1002/2016TC004447

Molnar, N. E., Cruden, A. R., & Betts, P. G. (2018). Unzipping continents and the birth of microcontinents. *Geology*, *46*(5), 451–454. https://doi.org/10.1130/G40021.1

Moore, A. M. G., Stagg, H. M. J., & Norvick, M. S. (2000). Deep-water Otway Basin: A new assessment of the tectonics and hydrocarbon prospectivity. *The APPEA Journal*, 66–85.

Moore, D. H., Betts, P. G., & Hall, M. (2016). Constraining the VanDieland microcontinent at the edge of East Gondwana, Australia. *Tectonophysics*, *687*, 158–179. https://doi.org/10.1016/j.tecto.2016.09.009

Morley, C. K., Haranya, C., Phoosongsee, W., Pongwapee, S., Kornsawan, A., & Wonganan, N. (2004). Activation of rift oblique and rift parallel pre-existing fabrics during extension and their effect on deformation style: examples from the rifts of Thailand. *Journal of Structural Geology*, *26*(10), 1803–1829.

https://doi.org/10.1016/j.jsg.2004.02.014

Müller, R. D., Seton, M., Zahirovic, S., Williams, S. E., Matthews, K. J., Wright, N. M., et al. (2016). Ocean Basin Evolution and Global-Scale Plate Reorganization Events Since Pangea Breakup. *Annual Review of Earth and Planetary Sciences*, *44*(1), 107–138. https://doi.org/10.1146/annurev-earth-060115-012211

Norvick, M. S., & Smith, M. S. (2001). Mapping the plate tectonic reconstruction of southern and southeastern Australia and implications for petroleum systems. *The APPEA Journal*, *41*, 15–35.

Peace, A., McCaffrey, K., Imber, J., van Hunen, J., Hobbs, R., & Wilson, R. (2018). The role of pre-existing structures during rifting, continental breakup and transform system development, offshore West Greenland. *Basin Research*, *30*(3), 373–394. https://doi.org/10.1111/bre.12257

Philippon, M., Willingshofer, E., Sokoutis, D., Corti, G., Sani, F., Bonini, M., & Cloetingh, S. (2015). Slip re-orientation in oblique rifts. *Geology*, *43*(2), 147–150. https://doi.org/10.1130/G36208.1

Philippon, Mélody, & Corti, G. (2016). Obliquity along plate boundaries. *Tectonophysics*, *693*, 171–182. https://doi.org/10.1016/j.tecto.2016.05.033

Phillips, T. B., & McCaffrey, K. J. W. (2019). Terrane Boundary Reactivation, Barriers to Lateral Fault Propagation and Reactivated Fabrics: Rifting Across the Median Batholith Zone, Great South Basin, New Zealand. *Tectonics*, *38*(11), 4027–4053. https://doi.org/10.1029/2019TC005772

Phillips, T. B., Jackson, C. A. L., Bell, R. E., Duffy, O. B., & Fossen, H. (2016). Reactivation of intrabasement structures during rifting: A case study from offshore southern Norway. *Journal of Structural Geology*, *91*, 54–73. https://doi.org/10.1016/j.jsg.2016.08.008

Power, M. R., Hill, K. C., Hoffman, N., Bernecker, T., & Norvick, M. (2001). The Structural and Tectonic Evolution of the Gippsland Basin: Results from 2D Section Balancing and 3D Structural Modelling. In K. C. Hill & T. Bernecker (Eds.), *Eastern Australasian Basins Symposium* (pp. 373–384). Melbourne: Petroleum Exploration Society of Australia.

Power, M. R., Hill, K. C., & Hoffman, N. (2003). Structural inheritance, stress rotation, overprinting and compressional reactivation in the Gippsland Basin - Tuna 3D seismic dataset. *The APPEA Journal*, *43*, 197–221. https://doi.org/https://doi.org/10.1071/AJ02010

Pysklywec, R. N., & Cruden, A. R. (2004). Coupled crust-mantle dynamics and intraplate tectonics: Two-dimensional numerical and three-dimensional analogue modeling. *Geochemistry, Geophysics, Geosystems*, *5*(10). https://doi.org/10.1029/2004GC000748

Ramberg, H. (1967). *Gravity, Deformation and the Earth's Crust, as Studied by Centrifuged Models*. London: Academic Press.

Ranalli, G. (1995). *Rheology of the Earth* (2nd ed.). London: Chapman and Hall.

Ranalli, G. (2001). Experimental tectonics: From Sir James Hall to the present. *Journal of Geodynamics*, *32*(1–2), 65–76. https://doi.org/10.1016/S0264-3707(01)00023-0

Riller, U., Cruden, A. R., Boutelier, D., & Schrank, C. E. (2012). The causes of sinuous crustal-scale deformation patterns in hot orogens: Evidence from scaled analogue experiments and the southern Central Andes. *Journal of Structural Geology*, *37*, 65–74. https://doi.org/10.1016/j.jsg.2012.02.002

Roberts, A. M., & Holdsworth, R. E. (1999). Linking onshore and offshore structures: Mesozoic extension in the Scottish Highlands. *Journal of the Geological Society*, *156*, 1061–1064.

Samsu, A., Cruden, A. R., Hall, M., Micklethwaite, S., & Denyszyn, S. W. (2019). The influence of basement faults on local extension directions: Insights from potential field geophysics and field observations. *Basin Research*, *31*(4), 782–807. https://doi.org/10.1111/bre.12344

Samsu, A., Cruden, A. R., Micklethwaite, S., Grose, L., & Vollgger, S. A. (2020). Scale matters: The influence of structural inheritance on fracture patterns. *Journal of Structural Geology*, *130*(September 2019), 103896. https://doi.org/10.1016/j.jsg.2019.103896

Schellart, W. P. (2000). Shear test results for cohesion and friction coefficients for different granular materials: Scaling implications for their usage in analogue modelling. *Tectonophysics*, *324*(1–2), 1–16. https://doi.org/10.1016/S0040-1951(00)00111-6

Schueller, S., & Davy, P. (2008). Gravity influenced brittle-ductile deformation and growth faulting in the lithosphere during collision: Results from laboratory experiments. *Journal of Geophysical Research: Solid Earth*, *113*(12), 1–21. https://doi.org/10.1029/2007JB005560

Schueller, S., Gueydan, F., & Davy, P. (2005). Brittle-ductile coupling: Role of ductile viscosity on brittle fracturing. *Geophysical Research Letters*, *32*(10), 1–4. https://doi.org/10.1029/2004GL022272

Schueller, S., Gueydan, F., & Davy, P. (2010). Mechanics of the transition from localized to distributed fracturing in layered brittle-ductile systems. *Tectonophysics*, *484*(1–4), 48–59. https://doi.org/10.1016/j.tecto.2009.09.008

Sharples, W., Moresi, L.-N., Jadamec, M. A., & Revote, J. (2015). Styles of rifting and fault spacing in numerical models of crustal extension. *Journal of Geophysical Research: Solid Earth*, *120*, 4379–4404. https://doi.org/10.1002/2014JB011813.Received

Tommasi, A., & Vauchez, A. (2001). Continental rifting parallel to ancient collisional belts: an effect of the mechanical anisotropy of the lithospheric mantle. *Earth and Planetary Science Letters*, *185*(1–2), 199–210. https://doi.org/10.1016/S0012-821X(00)00350-2

Vollgger, S. A., & Cruden, A. R. (2016). Mapping folds and fractures in basement and cover rocks using UAV photogrammetry, Cape Liptrap and Cape Paterson, Victoria, Australia. *Journal of Structural Geology*, *85*, 168–187. https://doi.org/10.1016/j.jsg.2016.02.012

Wijns, C., Weinberg, R., Gessner, K., & Moresi, L. (2005). Mode of crustal extension determined by rheological layering. *Earth and Planetary Science Letters*, *236*, 120–134. https://doi.org/10.1016/j.epsl.2005.05.030

Willcox, J. B., & Stagg, H. M. J. (1990). Australia's southern margin: a product of oblique extension. *Tectonophysics*, *173*, 269–281. https://doi.org/10.1016/0040-1951(90)90223-U

Willcox, J. B., Colwell, J. B., & Constantine, A. E. (1992). New ideas on Gippsland Basin regional tectonics. In *Gippsland Basin Symposium 22-23 June 1992* (pp. 93–110). Melbourne.

Williams, S. E., Whittaker, J. M., & Müller, R. D. (2011). Full-fit, palinspastic reconstruction of the conjugate Australian-Antarctic margins. *Tectonics*, *30*(6). https://doi.org/10.1029/2011TC002912

Wilson, J. T. (1966). Did the Atlantic Close and then Re-open? *Nature*, *211*, 676–681.

Wilson, R. W., Holdsworth, R. E., Wild, L. E., McCaffrey, K. J. W., England, R. W., Imber, J., & Strachan, R. A. (2010). Basement-influenced rifting and basin development: a reappraisal of post-Caledonian faulting patterns from the North Coast Transfer Zone, Scotland. *Geological Society, London, Special Publications*, *335*(1), 795–826. https://doi.org/10.1144/SP335.32

Withjack, M., & Jamison, W. R. (1986). Deformation produced by oblique rifting. *Tectonophysics*, *126*, 99–124. https://doi.org/https://doi.org/10.1016/0040-1951(86)90222-2

Zwaan, F., & Schreurs, G. (2017). How oblique extension and structural inheritance influence rift segment interaction: Insights from 4D analog models. *Interpretation*, *5*(1), SD119–SD138. https://doi.org/10.1190/INT-2016-0063.1